 doi:10.20944/preprints202010.0448.v1

Article

Application of a low-cost cellulose-based bioadsorbent for the effective recovery of terbium ions from aqueous solutions

Lorena Alcaraz [1], Dayana Nathaly Saquinga [2], Floralba López[2], Lola de Lima [2], Francisco J. Alguacil [1], Esther Escudero[1] and Félix A. López [1,*]

[1] National Center for Metallurgical Research (CENIM), Spanish National Research Council (CSIC) Avda. Gregorio del Amo 8, 28040 Madrid, España; alcaraz@cenim.csic.es (L.A.), fjalgua@cenim.csic.es (F.J.A.), f.lopez@csic.es (F.A.L.), Esther Escudero (mebaquero@cenim.csic.es)(E.E.B.)

[2] Yachay Tech University, School of Chemical Sciences & Engineering, Hacienda San José s/n, de San Miguel de Urcuquí, Ecuador; dayana.saquinga@yachaytech.edu.ec (D.S.), flopez@yachaytech.edu.ec (F.L.), ldelima@yachaytech.edu.ec (L.L.)

* Correspondence: f.lopez@csic.es (F.A.L.)

Abstract: Preparation of a low-cost cellulose-based bioadsorbent from the cellulosic material extracted from the rose stems (CRS) was carried out; rose stems were considered agricultural wastes. After the required pretreatment of this waste, and its further treatment with an acidic mixture of acetic and nitric acids, the CRS product was yielded. The resulting bioadsorbent was characterized by several techniques, such as X-ray diffraction, which revealed diffraction maxima related to cellulose structure, whose calculated crystallinity index (CrI) was 75 %. In addition, Fourier Transform Infrared spectroscopy (FTIR), ^{13}C Nuclear Magnetic Resonance (NMR), and X-ray Photoelectron Spectroscopy (XPS) showed signs of acetylation of the sample, also, the thermal properties of the solid was evaluated through Thermogravimetric Analysis (TGA). Scanning Electron Microscopy (SEM) showed cellulose fibers before and after the adsorption process, some particles with not regular shapes were also observed. The CRS bioadsorbent was used in the effective adsorption of valuable Tb(III) from aqueous solution. The adsorption data resulted in a better fit to the Freundlich isotherm, and pseudo-second-order kinetic models; however, chemisorption had not been ruled out. Finally, desorption experiments revealed a recovery of terbium ions with an efficiency of 97 % from terbium-loaded bioadsorbent.

Keywords: Cellulose; agricultural waste; bioadsorbent; rare earth; terbium adsorption-desorption

1. Introduction

Under the term of rare earth elements (REEs), 17 metals are included, all presenting similar chemical characteristics, which make them key components in the development of smart technologies and products associated with these. Also, and due to these similarities, making it difficult the separation between them. Being China the main producer of these REEs, and also being the country which keeps almost all the REEs reserves, there is a great concern, among Western countries, about the availability of these strategic elements, when, in addition, China is cutting their export. All the above led to the EU considering these elements of the utmost necessity, increasing the demand of their recycling from different sources, which is nowadays known as urban mining.

After leaching, these REEs are recovered from the solutions by different separation technologies, including precipitation, liquid-liquid extraction, ion exchange resins, etc. Of all of them, adsorption is one of the most popular methods [1,2], due to easiness in the perform, the possibility of treatment of dilute-metal solutions and/or unclarified solutions, etc., moreover, there is a myriad of potential

 doi:10.20944/preprints202010.0448.v1

adsorbents, some of them produced at a cheap rate and from secondary wastes, which eliminate the dumping associated with these wastes and add a further profit to them.

In the case of terbium, some adsorbents associated to its recovery from solutions included: 1-(2-pyridylazo)-2-naphthol (PAN) doped hybrid silica [3], nanoporous calcium alginate/carboxymethyl chitosan microbiocomposite powder containing $Ni_{0.2}Zn_{0.2}Fe_{2.6}O_4$ magnetic nanoparticles [4,5], magnetic CMC bionanocomposite containing a novel biodegradable nanoporous polyamide [6], lignocellulosic biomass [7], calcium alginate/poly(pyrimidine-thiophene-amide) [8], graphite nanoplatelets/magnetite [9], hydroxyapatite/$NiFe_2O_4$ composite [10], torrefied poplar-biomass [11], nZVI-montmorillonite [12].

As above mentioned, one of the features of adsorption processes is the potential use of a variety of adsorbents for any particular role, one type of these adsorbents is the biomass associated with agricultural wastes, that with a convenient treatment allows harnessing of lignocellulosic material leading to an interesting alternative for waste management because of the cost of the raw materials is reduced. In order to develop biomass-based adsorbents to recovery elements present in aqueous solutions, which represent an ecological and environmentally friendly process, different studies have reported the exploitation of the most abundant on earth natural biopolymer, cellulose [13,14], which along with lignin and hemicellulose, it is found in the cell wall of plants [15]. Cellulose biopolymer consists of D-glucopyranose repeating units linked by β-1,4-glycosidic bonds [16], and it is composed of amorphous and crystalline parts, the latter formed due to its hydrogen bonds between the hydroxyl groups of the cellulose structure [17]. Different sources have been reported for cellulose extraction such as wood, rice husk, pineapple leaf, kenaf, cane bagasse, etc. [18,19]; however, cellulose fibers extracted from the rose stems are scarcely investigated as potential adsorbents for metals.

The purpose of this work is to synthesize a low-cost cellulose-based bioadsorbent (CRS) from the treatment of rose stems with a mixture of acetic-nitric acids. After characterizing the bioadsorbent with various techniques including XRD, FTIR, TGA, NMR, XPS, and EDS, it is used as an adsorbent to investigate the adsorption efficiency against Tb(III), depending on pH, adsorbent dosage, and contact time, by performing a series of batch experiments. Various kinetic and isotherm models are tested for fitting the experimental data. Thermodynamic parameters (ΔS^0, ΔG^0, and ΔH^0) are also estimated to find further characteristics of the adsorption process. Metal desorption from Tb(III)-loaded bioadsorbent is also investigated using acidic solutions. To the best of our knowledge, the use of the CRS bioadsorbent has not been investigated for Tb(III) adsorption.

2. Materials and Methods

2.1. From the rose stems to the CRS bioadsorbent

Rose stems were used as biomass sources to extract cellulose. Initially, they were washed, cut into small pieces, and dried in the oven at 50 °C for 2 days. Then, the stems were ground and sieved to obtain the precursor. Approximately, 5 g of the precursor was treated with a mixture of acetic acid: nitric acid (v/v, 10:1) and it was mixed with a glass rod. After that, the beaker that contains the mixture was placed in a sand bath at a temperature of 110 - 120 °C for 20 min. It was allowed to cool at room temperature, then it was filtered and washed with distilled water until reaching a neutral pH. Finally, the solid was dried at 60 °C obtaining the bioadsorbent, which was labeled as CRS. Research manuscripts reporting large datasets that are deposited in a publicly available database should specify where the data have been deposited and provide the relevant accession numbers. If the accession numbers have not yet been obtained at the time of submission, please state that they will be provided during review. They must be provided prior to publication.

2.2. Characterization of the bioadsorbent

Structural characterization was performed by X-ray Diffraction (XRD). Diffractograms were taken using a Rigaku Miniflex 600 X-ray diffractometer, using a monochromatic Cu Kα radiation source (λ = 0.1539 nm), 40 kV and 20 mA in a range from 10° to 40° with a scanning time of 25 min. Furthermore,

Preprints (www.preprints.org) | NOT PEER-REVIEWED | Posted: 22 October 2020 doi:10.20944/preprints202010.0448.v1

the crystallinity index (CrI, %) was calculated according to the method proposed elsewhere [20], using the following Equation 1:

$$\text{CrI}\ (\%) = \frac{(I_{002} - I_{AM})}{I_{002}} \text{ x } 100, \qquad \text{(Eq. 1)}$$

where, I_{002} was the maximum intensity corresponding to the (002) plane, and IAM represents the intensity of the diffraction peak at 2θ = 18° [20]. Thermogravimetric / Differential Thermal Analysis (TG/DTA) thermograms were obtained using a differential thermal analyzer from 20 to 600 °C at a 10 °C/min heating rate. In addition, as an inert medium helium gas was used, and the reference material was aluminum oxide. Chemical and morphological characterization were performed by Scanning Electron Microscopy (SEM), and by different spectroscopic techniques, such as Fourier Transform Infrared (FTIR), Nuclear Magnetic Resonance (NMR), X-ray Photoelectron Spectroscopy (XPS) techniques. FTIR measurements were performed using Varian 670-IR Spectrometer with 32 scans in the range from 400 to 4000 cm^{-1} and a resolution of 4 cmv. Measurements were carried out on pellets formed by a mixture of the grounded solid and potassium bromide (KBr). The textural characterization of the solid was analyzed by the physical adsorption of nitrogen at 77 K using Micromeritics ASAP 2010, the study of the resulting Brunauer-Emmett-Teller (BET) isotherm allowed to determine the values of parameters such as specific surface area, pore-volume, and pore size. NMR spectra of CRS were taken on a BRUKER NMR Spectrometer 400 MHz using Cross Polarization Magic Angle Spinning (CP-MAS) and High Power 1H Decoupling techniques. XPS measurements were carried out using a Fisons MT500 spectrometer (Fison Instrument, East Grinstead, UK) operated at 300 W equipped with a hemispherical electron analyzer (CLAM2) and a non-monochromatic Mg K**α** X-ray source. Spectra were collected at pass energy of 20 eV (typical for high-resolution conditions). The area under each peak was calculated fitting the experimental curve to a variable proportions combination of Lorentzian and Gaussian lines. Binding energies were calibrated to the C1s peak at 285.0 eV. SEM images were obtained using a JSM 6335F microscope operated in secondary electron mode with an accelerating voltage of 15 kV. For SEM observation, samples were previously coated with gold for 50 seconds using a Q150RS QUORUM-Rotary Pumped Coater. Energy dispersive spectroscopy (EDS) analyses were carried out by using an OXFORD INCA instrument.

2.3. Adsorption experiments

Terbium adsorption by the CRS sample was carried out using batch experiments. Initially, the stock solution of 50 mg/L metal concentration was prepared dissolving terbium nitrate hexahydrate ($Tb(NO_3)_3{\cdot}6H_2O$, Panreac) in MilliQ water. Then, the stock solution was diluted to obtain solutions of 10 mg/L concentration. Different experiments were carried out in a Selecta Termotronic thermostat-controlled bath, equipped with multiple Lab Companion MS-52M stirrers. To determine the adsorption capacity of both samples, different adsorption tests will be carried out, where parameters such as contact time, temperature, pH, and amount of adsorbent were varied. Aliquots of 1 mL were collected at elapsed times and filtered through a filter-provided syringe. The pH of the solutions was adjusted with HCl (0.12 M). Terbium concentrations in the solutions were determined by Inductively Coupled Plasma-Optical Emission Spectrometry (ICP-OES) using an Agilent ICP-OES model 5100 VDV, being the associated analytical error of ±2%.

The adsorption capacity (q_t (mg/g)) was defined by Equation 2:

$$q_t = \frac{(c_0 - c_t)\cdot V}{m}, \qquad \text{(Eq. 2)}$$

where c_o and c_t (mg/L) are the initial and at elapsed time terbium concentrations in the solution, respectively; V (L) is the volume of the solution, and m (g) is the mass of the adsorbent used in each adsorption process.

The adsorption data were analyzed using the linear equations of Langmuir, Freundlich, and Temkin models [21,22] (Equations 3 to 5, respectively):

$$\frac{C_e}{q_e} = \frac{1}{q_m \cdot b} + \frac{1}{q_m} \cdot c_e, \qquad \text{(Eq. 3)}$$

Preprints (www.preprints.org) | NOT PEER-REVIEWED | Posted: 22 October 2020 doi:10.20944/preprints202010.0448.v1

$$\ln q_e = \ln k_F + \frac{1}{n} \cdot \ln c_e \ , \qquad \text{(Eq. 4)}$$

$$q_e = B \cdot \ln A_T + B \cdot \ln c_e \ , \qquad \text{(Eq. 5)}$$

where c_e (mg/L) represents the concentration of terbium in solution at equilibrium; q_e (mg/g) is the adsorbed terbium amount by mass of the adsorbent; q_m (mg/g) is the maximum terbium adsorbed amount by mass of the adsorbent and b (L/mg) is the Langmuir constant; K_F (mg/g)·(L/mg) and n (dimensionless) are the Freundlich constants which are indicative of the adsorption capacity and adsorption intensity, respectively. A_T (L/g) and B (J/mol) are the Temkin isotherm equilibrium binding and Temkin isotherm constants, respectively.

Adsorption kinetics were determined using the pseudo-first [23], pseudo-second [24], Elovich [24] and Bangham [25] models (Equations 6 to 9):

$$\ln(q_e - q_t) = \ln q_e - k_1 \cdot t \ , \qquad \text{(Eq. 6)}$$

$$\frac{t}{q_t} = \frac{1}{k_2 \cdot q_e^2} + \frac{1}{q_e} \cdot t \ , \qquad \text{(Eq. 7)}$$

$$q_t = \frac{1}{\beta}(\ln \alpha\beta) + \frac{1}{\beta \ln t} \ , \qquad \text{(Eq. 8)}$$

$$q_t = \ln k_B + \frac{1}{m} \ln t \ , \qquad \text{(Eq. 9)}$$

where k_1 (min^{-1}) and k_2 (g/min·mg) correspond to the first-order and second-order adsorption constants, respectively, and α and β were related to the rate and the activation energy for the chemisorption.

In order to analyze the rate law which governing the adsorption process, three different possible adsorption mechanisms were studied [26]: particle diffusion model (intraparticle or internal diffusion; the diffusion of Tb(III) within the bioadsorbent), film diffusion model (bulk diffusion and external film diffusion; diffusion of the Tb(III) ions from the aqueous solution to the bioadsorbent surface), and the moving boundary process (Equations 10 to 12 respectively):

$$\ln(1 - F^2) = -k \cdot t \ , \qquad \text{(Eq. 10)}$$

$$\ln(1 - F) = -k \cdot t \ , \qquad \text{(Eq. 11)}$$

$$3 - 3 \cdot \left(1 - F^{2/3}\right) - 2 \cdot F = k \cdot t \ , \qquad \text{(Eq. 12)}$$

where k (min^{-1}) was the corresponding constant, and F (dimensionless) is calculated according to Equation 13:

$$F = {[Tb^{3+}]_t}/{[Tb^{3+}]_{eq}}, \qquad \text{(Eq. 13)}$$

In the last equation, $[Tb^{3+}]_t$ and $[Tb^{3+}]_{eq}$ (mg/L) represent the concentrations of metal adsorbed after an elapsed time and at equilibrium, respectively.

The activation energy (E_a) was calculated from the Arrhenius equation (Equation 14):

$$k = A \cdot e^{-E_a/R \cdot T} \ , \qquad \text{(Eq. 14)}$$

where R (kJ/mol·K) is the universal gas constant and T (K) is the absolute temperature.

2.4. Desorption experiments

Desorption experiments were carried out using the filtered solids (designated as CRS-Tb) previously subjected to the adsorption process. Desorption solution (the type of eluent, and its concentration) as well as the ratio of volume of the solution / CRS-Tb dosage were investigated. CRS-Tb solids were put into contact with different desorption solutions (HCl 0.2 M, HCl 0.5 M, and H2SO4

 doi:10.20944/preprints202010.0448.v1

0.2 M) at different ratios of volume of the eluent to CRS-Tb dosage (1250, 2500, and 5000 mL/g) at 25 °C for 4 h.

3. Results and discussion

3.1. Characterization of the bioadsorbent

Figure 1 shows the XRD pattern for the CRS sample. XRD diffraction maxima are recorded at 2θ values of around 15°, 16°, 22°, and 34°. These peaks are characteristic of the cellulose and can be attributed to the crystalline planes (hkl) (101), (10-1), (002), and (040), respectively, attributed to cellulose I crystal structure [20,27,28]. Furthermore, the crystallinity index (CrI) was calculated using Equation 1, resulting in a 75% for CRS. The obtained % CrI is lower than the value for standard cellulose reported in the literature [29], this result being probably due to the contribution of the amorphous part associated with the cellulose structure or with other lignocellulosic structures.

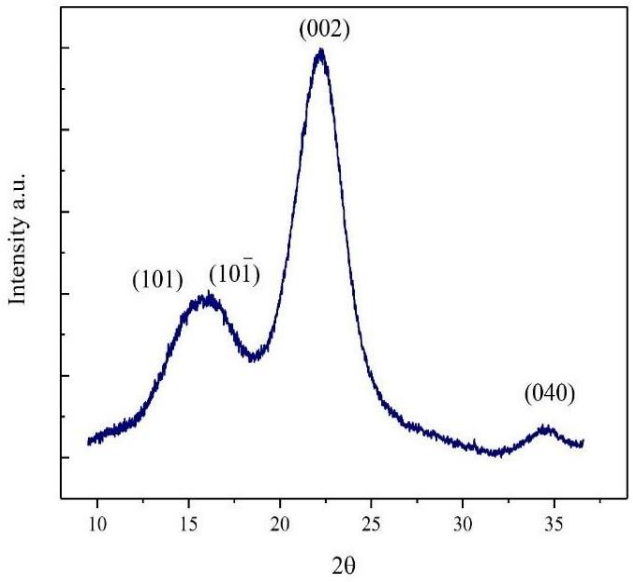

Figure 1. XRD patterns for the CRS sample, indicating the different crystalline planes associated.

The FTIR spectrum of the CRS sample is shown in Figure 2. The recorded spectrum shows characteristic bands of cellulose structure, such as the peak located at 3401 cm^{-1} which correspond to the stretching of O-H groups, and the peak at 2902 cm^{-1} due to C-H stretching [30]. Furthermore, at 1430 cm^{-1} the bending mode of CH_2 groups is found, and the peak located at 1372 cm^{-1} indicates the O-H bending. The peak at 1162 cm^{-1} is associated with the antisymmetric bridge vibration, the peaks that appear in the region 1076-1023 cm^{-1} and the peak at 897 cm^{-1} indicate the C-O-C pyranose ring skeletal vibration and the β-glycosidic bond [30,31], respectively. Also, in 1640 cm^{-1} it can see the bending mode of the absorbed water [32].

In addition, spectrum for the CRS sample shows news peaks from those associated with pure cellulose, which are indicated in blue. The one located at 1735 cm^{-1} corresponds to the C=O vibration associated with the ester group [33]. This peak is related to the bioadsorbent yielded after the treatment under acidic conditions to which the precursor is subjected, indicating acetylation of the cellulose. Also, two other peaks appearing at 1505 cm^{-1} and 1256 cm^{-1} suggest that lignin and hemicellulose are still present in the structure of cellulose sample obtained [34,35].

Preprints (www.preprints.org) | NOT PEER-REVIEWED | Posted: 22 October 2020 doi:10.20944/preprints202010.0448.v1

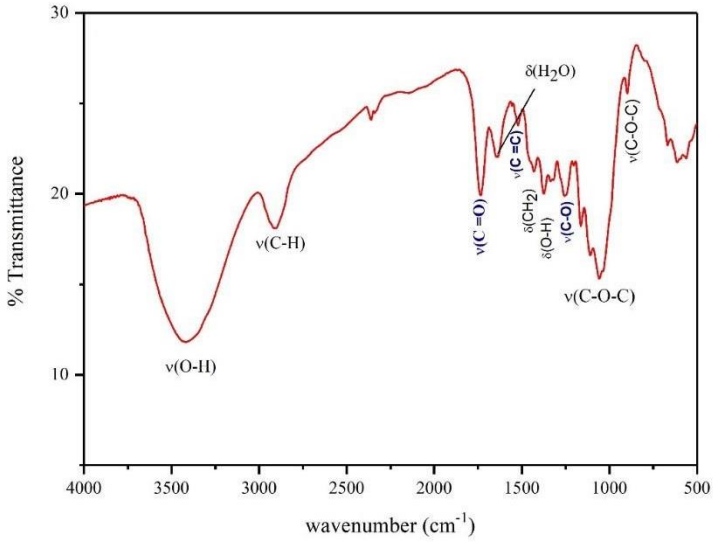

Figure 2. FTIR spectrum of the CRS sample obtained, indicating the assignment of the different appearing peaks.

Further, the experimental data of textural characterization was fitted by the BET model to obtain the information about the surface feature of the adsorbent. As it can see in Figure 3(a), the resultant adsorption-desorption isotherm corresponds to Type IV BET isotherm. This type of isotherm is characteristic of mesoporous solids, with a pore diameter between 2 nm and 50 nm. In addition, the formation of multilayers and the hysteresis loop are observed [15,36]. From the BET model the values for total specific surface area (S_{BET}), pore-volume (V_T), and pore diameter distribution (D_P) were determined. The value obtained for S_{BET} was 1.83 $m^2 \cdot g^{-1}$, for V_T was 0.0036 $cm^3 \cdot g^{-1}$, and for D_P distribution covers a range between 12 - 55 Å (1.2 - 5.5 nm) as shown in Figure 3(b).

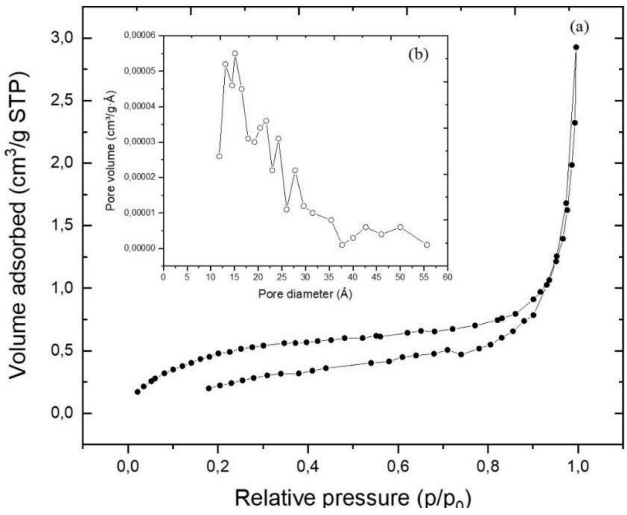

Figure 3. (a) Experimental plot for adsorption-desorption BET isotherm obtained for CRS sample, and in the inset (b) the pore size distribution is shown.

Thermogravimetric analysis was carried out to evaluate the thermal stability of the obtained bioadsorbent. Figure 4 shows the TG and DTG curves. In the DTG curve three peaks appear: the first one, occurring between 50 and 120 °C, corresponds to the elimination of the adsorbed water and the solvents used for the bioadsorbent obtaining [37,38]; the next step of degradation is attributed to the

Preprints (www.preprints.org) | NOT PEER-REVIEWED | Posted: 22 October 2020 doi:10.20944/preprints202010.0448.v1

decomposition of hemicellulose structures, which usually occurred in the 220 - 315 °C range [39]; finally, the main stage of degradation corresponds to the depolymerization of cellulose. According to literature, the decomposition of cellulose is found in the 315 - 400 °C range, with a maximum peak at 355 °C [39,40]. In the present case, this maximum was established at 321 °C. The slight shift could be related to the variation of the crystallinity of the evaluated sample and compared to the one reported in the literature [39,40].

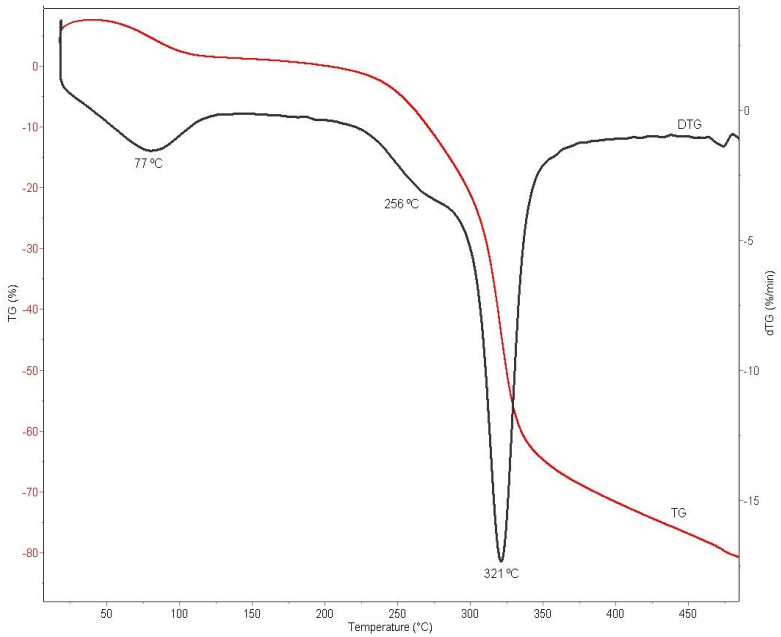

Figure 4. DTG curve obtained for the CRS sample.

In the NMR spectrum obtained for the CRS sample, the peaks labeled from C1 to C6 in Figure 5 are characteristic of cellulose structure, and they are indicated in the inset of the figure. The two peaks appearing at 62.56 and 64.89 ppm are attributed to carbon six (C6), and correspond to amorphous and crystalline parts in the cellulose structure, respectively [30,41]. The group of peaks from 72.09 to 74.74 ppm is due to C2, C3, and C5, the two peaks at 83.54 and 88.74 ppm correspond to C4, due to the crystalline and the amorphous part of cellulose, respectively [42,43], and C1 has associated the peak appearing at 104.89 ppm [30,44]. The two additional signals at 171.93 ppm (C7) and 21.13 ppm (C8) are related to the acetylation of cellulose during the extraction process, and it is consistent with the information provided by FTIR analysis.

It is worth to mention here, that the OH group on C6 in cellulose is a primary carbon, and is being considered the most reactive, and the one presenting less steric hindrance compared to OH groups located on C2 and C3, which are secondary carbons. Therefore, most reactions are more likely to occur through C6 [45,46].

Preprints (www.preprints.org) | NOT PEER-REVIEWED | Posted: 22 October 2020 doi:10.20944/preprints202010.0448.v1

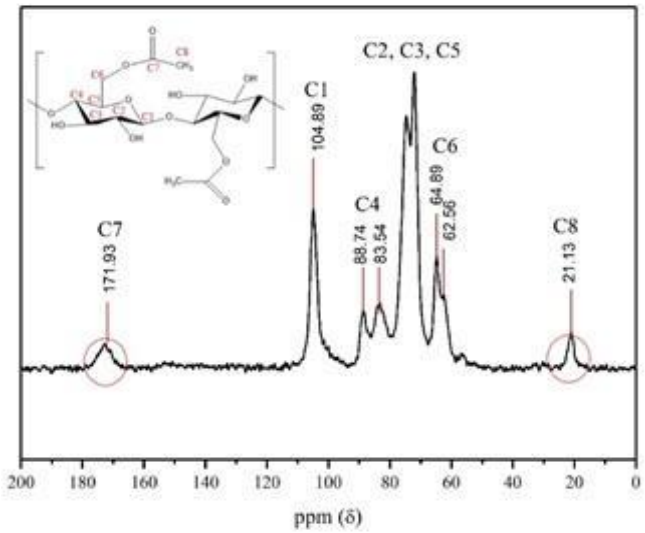

Figure 5. ^{13}C NMR with CP-MAS spectrum for the CRS sample, indicating the different carbon types present in the CRS structure.

Figure 6 shows the C1s, O1s and N1s XPS spectra for the CRS sample. C1s spectrum exhibits four signals corresponding to the chemical bonding state of carbon atoms with other atoms. The first one located at a binding energy of 285 eV corresponds to C-H or C-C groups, while the next signals appearing at 286.9 and 288.1 eV are attributed to C-O group, the next signal is attributed to O-C-O/C=O bonds, respectively, and the last one due to O-C=O at 289.1 eV in an ester group [47]. From this could be indicating that, according to the FTIR and NMR measurements, the acetylation of cellulose in the extraction process occurred. In addition, the higher intensity for the first peak compared to that occurring in the spectrum of pure cellulose previously reported attracts attention, it could be associated with the presence of impurities such as lignin or hemicellulose [48]. On the other hand, O1s spectrum shows three signals, the one located at 533 eV is associated with C-O group of the structure of cellulose itself, the other two signals at 531.3 eV and 529.6 eV correspond to C=O and O-C=O groups [49,50], respectively, this information is in accordance with the signals specified in C1s spectrum. In addition, CRS shows a signal in the nitrogen region at 400 eV, this occurs because traces of nitric acid used in the extraction process may be still present.

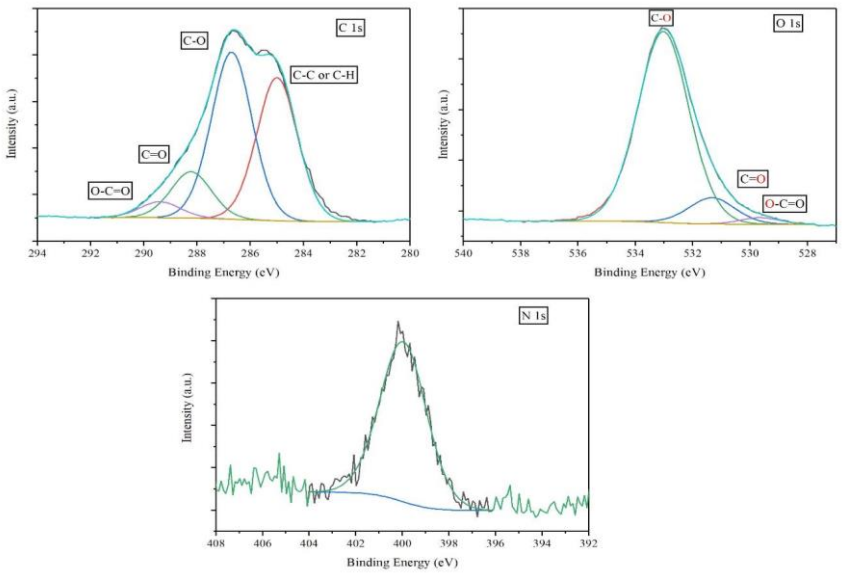

Figure 6. C1s, O1s and N1s XPS spectra of CRS samples, also showing the respective deconvolution curves.

Preprints (www.preprints.org) | NOT PEER-REVIEWED | Posted: 22 October 2020 doi:10.20944/preprints202010.0448.v1

The esterification process of the cellulose is consistent with a Fischer esterification reaction that, according to literature, occurs between a carboxylic acid and an alcohol in the presence of a catalyst to form an ester [51,52]. In this work, a reaction occurring between acetic acid and hydroxyl groups of cellulose is proposed and represented in Figure 7, in which HNO_3 acts as the catalyst in order to obtain the esterified cellulose, as well as water as a side product.

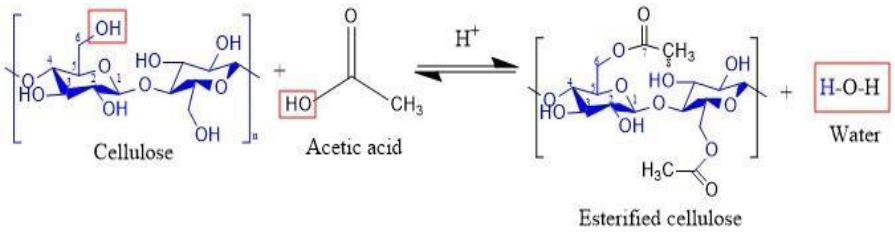

Figure 7. Representation of esterified cellulose obtaining by the Fischer esterification reaction.

The bioadsorbent surface before the adsorption process (CRS) and after the terbium adsorption (CRS-Tb) was studied by SEM microscopy. In Figure 8(a,b) are shown the SEM micrographs of both samples, in which the characteristic fibers of cellulose were observed. This fibrous structure is attributed to hydrogen bonds that hold together the cellulose chains [53]. The presence of particles with different sizes and shapes also observed, can be attributed to lignin and hemicellulose structures that persist in the fibers [44]. In addition, no significant differences were observed on the surface of the fibers in the SEM images before and after the adsorption process. However, as can be appreciated in Figure 8(c), EDS spectra for both samples exhibit some compositional differences. Despite that, as expected, the presence of carbon and oxygen elements were found in both samples, and EDS spectra registered for the CRS-Tb sample exhibited the presence of terbium element. This result indicated that the terbium adsorption onto the obtained CRS bioadsorbent was satisfactorily done.

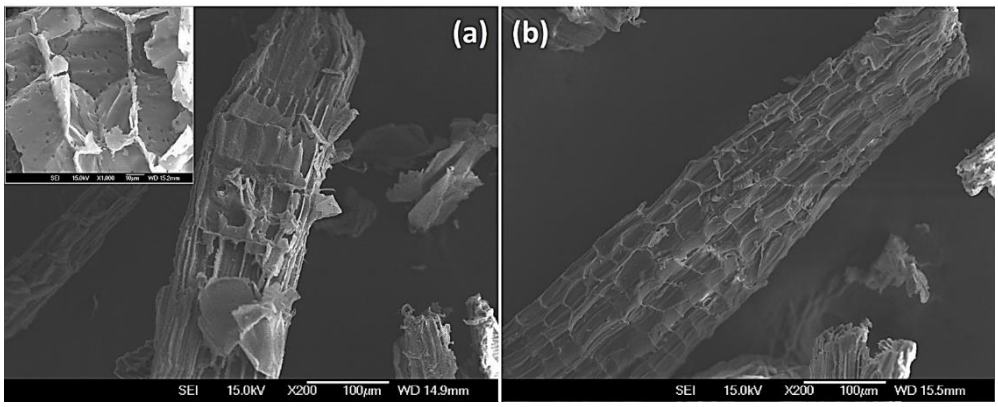

Preprints (www.preprints.org) | NOT PEER-REVIEWED | Posted: 22 October 2020 doi:10.20944/preprints202010.0448.v1

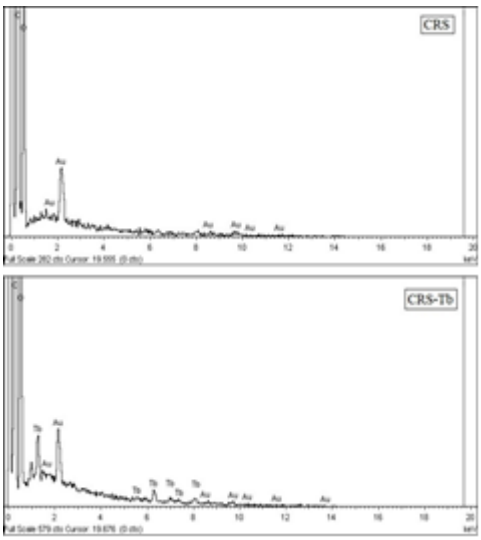

Figure 8. SEM images of the CRS bioadsorbent (a) before and (b) after the terbium adsorption. (c) EDS spectra of the unmodified sample (CRS) and sample after the adsorption of terbium (CRS-Tb).

3.2. Adsorption experiments

3.2.1. pH influence

To analyze the influence of the solution pH on Tb(III) adsorption on the bioadsorbent prepared, different experiments were carried out at 25 ºC, using terbium solutions of 10 mg/L concentration with 500 mg/L of the adsorbent. The evaluation of the effect of the pH in adsorption tests has great importance since it has an influence not only on the surface charge of the adsorbent, but also on the degree of ionization and the kind of species that the adsorbate forms in the solution [54]. However, only Tb^{3+} exists under acidic and near neutral pH values conditions (Figure 9).

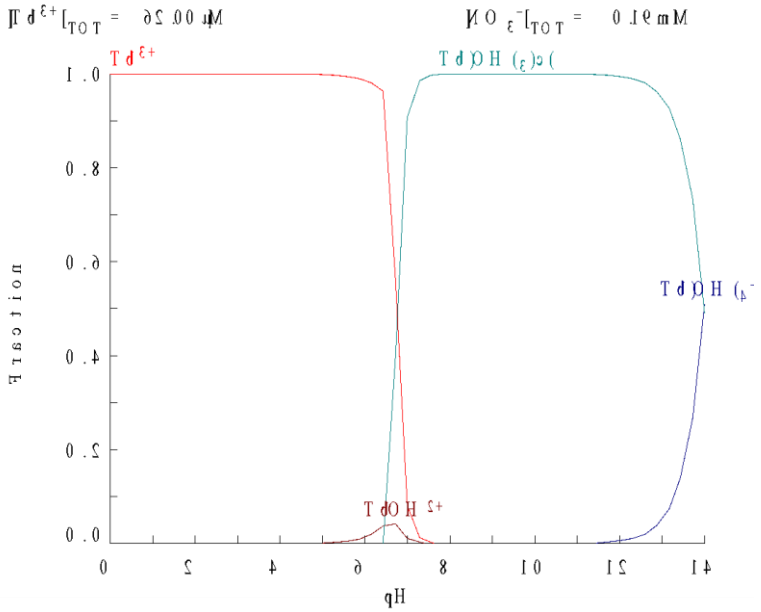

Figure 9. Terbium(III) speciation as a function of the pH values [55].

Figure 10 shows the adsorption capacity as a function of the contact time for the different pH values studied. It can be appreciated that the percentage of Tb(III) adsorption decreases as the pH value decreases, reaching a minimum value of 4 mg/g (corresponding to a 16 % of

Preprints (www.preprints.org) | NOT PEER-REVIEWED | Posted: 22 October 2020 doi:10.20944/preprints202010.0448.v1

adsorption) at pH 2, because the interaction between H^+ and Tb^{3+} for binding the active sites increases. The scarce protonation of the functional groups presented in the bioadsorbent, also inhibits the reaction between the bioadsorbent and Tb^{3+} species that could be of the utmost importance, for the low value of adsorption efficiency, as the pH of the solution decreases [56]. The influence of solution pH on Tb(III) adsorption was not investigated for pH values greater than 5 in order to prevent terbium ions precipitation as the hydroxides (Figure 9). Therefore, pH 5 was applied as an optimum value for further adsorption studies.

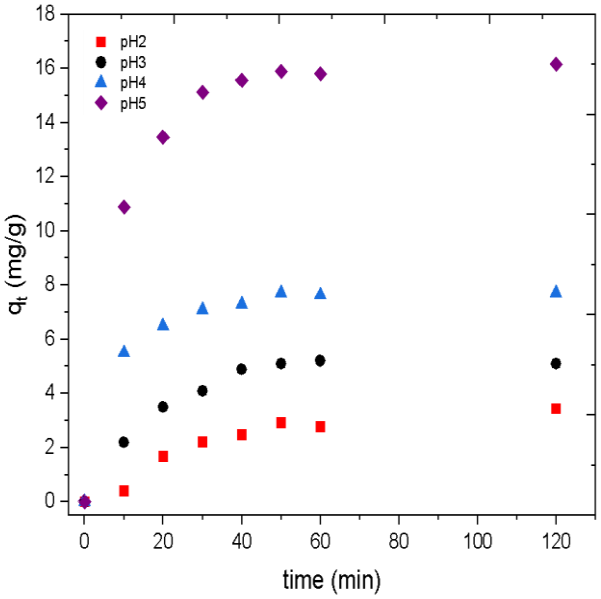

Figure 10. Influence of the solution pH in Tb(III) adsorption onto CRS at the different time tested.

3.2.2. Influence of the adsorbent dosage

The effect of different adsorbent dosages on Tb(III) adsorption was investigated using 250, 500, 750, and 1000 mg/L of the CRS at 25 ºC, using terbium solutions of 10 mg/L concentrations. Figure 11 shows the effect of this variation on the adsorption process, it is clearly seen that the Tb(III) concentration loaded onto the bioadsorbent decreases with the increment of the amount of adsorbent. Thus, for adsorbent doses of 250, 500, 750, and 1000 mg/L, the adsorption percentages were of 62 % (25 mg/g), 80 % (16 mg/g), 84 % (11 mg/g), and 92 % (9 mg/g), respectively. The values in parentheses correspond to the maximum amount (mg) of Tb(III) adsorbed per gram of adsorbent. These results can be attributed to that as the adsorbent concentration was increased, the available adsorbent sites were also increased; then, the percentage of metal adsorption increased. In addition, the adsorption significantly varied with the increase of the adsorbent dosage in the range 250 - 500 mg/L, while for the range 750 - 1000 mg/L of CRS, the metal concentrations onto the bioadsorbent were only slightly modified. The decrease in the adsorption capacity might be due to the interference that existed between the binding sites and adsorbate, or the insufficiency of Tb(III) in the solution with respect to available binding sites [57].

Preprints (www.preprints.org) | NOT PEER-REVIEWED | Posted: 22 October 2020 doi:10.20944/preprints202010.0448.v1

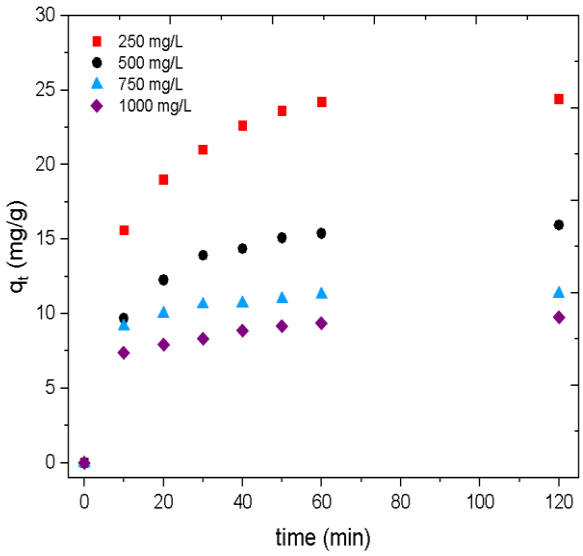

Figure 11. Tb(III) adsorption as a function of time for different CRS dosages tested.

3.2.3. Influence of the temperature

The effect of the temperature on terbium adsorption was investigated using aqueous solutions of 10 mg/L of terbium, at pH value of 5 with 500 mg/L of the CRS. The results of this study were shown in Figure 12. The adsorption capacity slightly increased with the temperature, obtaining around 16.0 mg/g to 25 ºC, 16.5 mg/g to 40 ºC, and 16.9 mg/g to 60 ºC. These results indicate that the temperature increase slightly improves the terbium adsorption process. However, equilibrium is reached earlier when the temperature increases indicating that the temperature quickens the adsorption process.

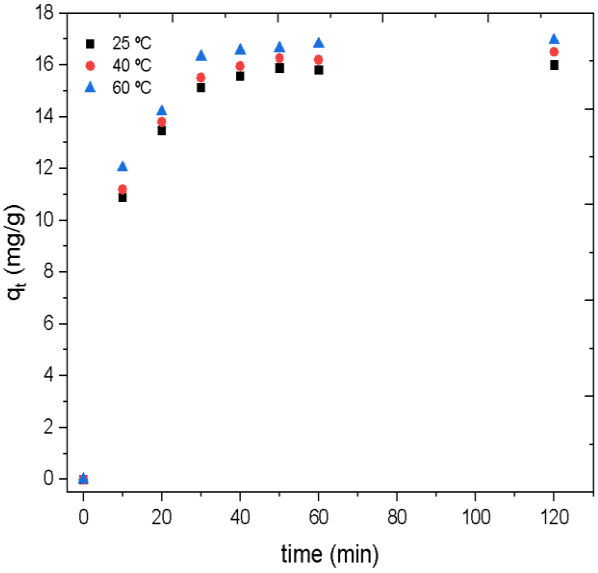

Figure 12. Influence of the temperature on Tb(III) uptake onto the adsorbent at the different time tested.

3.2.4. Adsorption isotherms

Experimental results of the adsorption process were fitted to various isotherm models using equations 3-5. Langmuir model assumes that on the surface of the adsorbent all sites are 'equally active'. Thus, the surface is energetically homogeneous. As a result, a monolayer surface is formed

Preprints (www.preprints.org) | NOT PEER-REVIEWED | Posted: 22 October 2020 doi:10.20944/preprints202010.0448.v1

without any interaction between the adsorbed molecules of the adsorbate [58,59]. The Freundlich model is valid for heterogeneous surfaces, which indicate that the adsorption energy exponentially decreases on the finishing point of the adsorption centers of an adsorbent [21,60]. The Temkin isotherm model takes into account the adsorbent-adsorbate interactions. This model assumes that, due to these interactions, the heat of adsorption would decrease with the coverage in the surface [58].

The correlation coefficients associated with fits to above mentioned models shown in Table 1, suggest that the Freundlich isotherm better describe the terbium adsorption onto CRS bioadsorbent. The calculated values of K_F and n were 10.1 (mg/g)·(L/mg) and 1.5, respectively. The positive value of n indicates that the adsorption process is favorable [21].

Table 1. Parameters and correlation coefficients obtained from fits of isotherm models to the experimental data.

Isotherm model	Parameters value	
Langmuir	q_m (mg/g)	48.47
	b (L/mg)	0.25
	R^2	0.9094
Freundlich	k_F (mg/g)·(L/mg)	10.07
	n (dimensionless)	1.57
	R^2	0.9823
Temkin	A_T (L/g)	1.04
	B (J/mol)	10.18
	R^2	0.9539

Table 2 shows the information reported about metal adsorption for several bioadsorbents prepared from different cellulose precursors under optimal conditions. It is worth mentioning here that most of the data presented in the Table 2 were obtained at pH of 6 and above, in which the metal was precipitated. Thus, the adsorption data given by the respective authors was not of a true cation adsorption process but of a precipitation process. So, the present work describes a one-step process to obtain a low-cost cellulose-based bioadsorbent obtained from rose stems, a precursor considered as agricultural waste, which is effective for terbium adsorption from aqueous solutions.

Table 2. Metal adsorption under optimal conditions for different cellulose-precursors used.

Cellulose precursor	Metal	pH	Maximum adsorption (mol/g)	Isotherm model	Kinetic model	Reference
Torrefied poplar-biomass	Tb(III)	4	0.06	Sips	pseudo-second-order	[11]
$KMnO_4$-modified pineapple bran	Cu(II)	7	0.11	Freundlich	pseudo-second-order	[61]
Thiol-functionalized cellulose acetate	Cu(II)	4	0.62	Langmuir	pseudo-second-order	[62]
Thiol-functionalized cellulose acetate	Cd(II)	4	0.27	Langmuir	pseudo-second-order	[62]
Thiol-functionalized cellulose acetate	Pb(II)	4	0.09	Langmuir	pseudo-second-order	[62]
Citric acid-modified cellulose from E. crassipes	Zn(II)	6	0.13	----	----	[63]

 doi:10.20944/preprints202010.0448.v1

Citric acid-modified cellulose from E. crassipes	Cu(II)	6	0.29	----	----	[63]
Citric acid-modified cellulose from E. crassipes	Cd(II)	6	0.38	----	----	[63]
Citric acid-modified cellulose from E. crassipes	Pb(II)	6	0.10	----	----	[63]
Bagasse pulp	Cu(II)	5	0.55	Freundlich	pseudo-second order	[64]
Thiourea-functionalized comercial cellulose	Eu(III)	---	0.18	Langmuir	pseudo-second-order	[65]
Thiourea-functionalized comercial cellulose	Nd(III)	---	0.51	Langmuir	pseudo-second-order	[65]
Rose stems	Tb(III)	5	0.16	Freundlich	pseudo-second order	This work

3.2.5. Kinetics studies

To analyze the kinetics of the adsorption process, the experimental data obtained at the different temperatures tested were plotted using different models (equations 6 to 9): pseudo-first-order, pseudo-second-order, Elovich, and Bangham. Their obtained correlation coefficients are summarized in Table 3. Experimental data in the temperature range of 25 - 60 ºC fit well to the pseudo-second order kinetic model [66], with k_2 value of 0.021 ± 0.002 g/min·mg. From the model data, the value of $q_{e,calc}$ is about 16.9 mg/g, which match well with the experimental values of near 16.5 mg/g.

Table 3. Summary of correlation coefficients corresponding to different kinetic models evaluated.

	20 °C	**40 °C**	**60 °C**
pseudo-first order	0.9791	0.9566	0.9579
pseudo-second order	0.9982	0.9983	0.9984
Elovich	0.9894	0.9838	0.9631
Bangham	0.9198	0.8898	0.8586

From these obtained results, Arrhenius equation parameters can be fitted using the kinetic constants. The plot of ln k versus 1/T yields a straight line, with slope $-E_a/R$. The magnitude of the activation energy is commonly used as the basis for differentiating between physisorption or chemisorption process. In the case of the physical adsorption process, the processes are reversible, equilibrium is rapidly achieved and the energy required is small (between the range of 5 - 40 kJ/mol). The chemical adsorption process is irreversible and involves stronger forces. For this, activation energies are larger (between 40 - 800 kJ/mol) [67]. The calculated activation energy was 5.71 kJ/mol suggesting that the terbium adsorption is a physical adsorption process.

The obtained adsorption results at 25 °C were analyzed to determine the possible rate law governing the adsorption of Tb(III) onto the adsorbent. Figure 13 shows the fitted obtained from equations 10 - 12. The obtained best fit (R^2 = 0.9957) was found for the particle diffusion-controlled process (Equation 10) for the present system [66], with a rate constant of 0.044 min^{-1}.

Preprints (www.preprints.org) | NOT PEER-REVIEWED | Posted: 22 October 2020 doi:10.20944/preprints202010.0448.v1

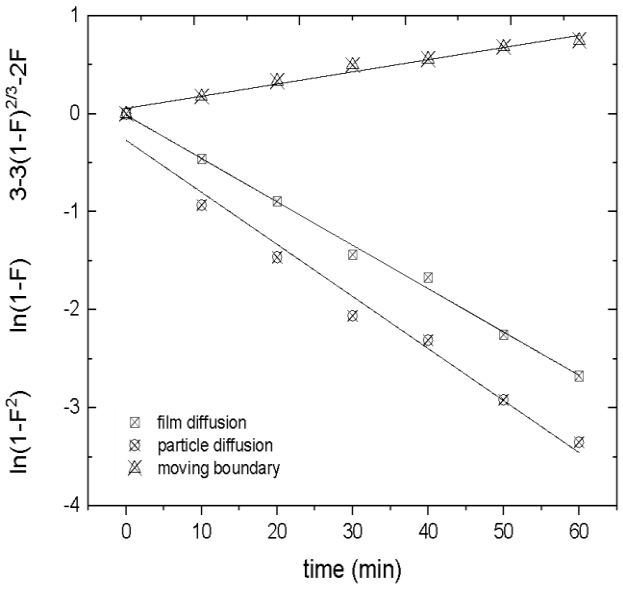

Figure 13. Adsorption mechanisms of Tb^{3+} on cellulose adsorbent.

3.2.6. Desorption experiments

Desorption experiments were performed with the CRS-Tb solids loaded with 16 mg Tb(III) per gram of bioadsorbent during 120 min. Table 4 summarized the results obtained under the different experimental conditions used in this work. The influence of different preparation conditions for desorption solutions on terbium desorption was investigated using 0.2 M H_2SO_4 and HCl solutions at ratios of 1250, 2500, and 5000 mL per gram of bioadsorbent. For a fixed concentration of the solution (0.2 M), a higher desorption percentage with the use of HCl was found. The maximum percentages were 63% - 75% and 72% - 81% for H_2SO_4 and HCl, respectively.

The effect of the HCl concentration (0.2 M and 0.5 M) was also investigated under the same experimental conditions. It can be appreciated that, the higher the acid concentration, the higher the desorption percentage, even achieving yields of 79 % - 97 %. Finally, regardless of the type of solution and the acid concentration used in the experiments, desorption percentage increases with the volume of the eluent/bioadsorbent amount (mL/g) ratio. The obtained results indicate that it is possible the effective recovery of terbium ions from Tb-loaded CRS with interesting yields.

Table 4. Terbium concentration in the eluent solution and desorption percentage for the different solutions tested.

	Volume solution per gram of bioadsorbent (mL/g)	**[Tb^{3+}] in the equilibrated solution (mg/L)**	**Desorption (%)**
H_2SO_4 (0.2 M)	1250	8.1	63
	2500	4.7	73
	5000	2.4	75
HCl (0.2 M)	1250	9.2	72
	2500	4.8	75
	5000	2.6	81
HCl (0.5 M)	1250	10.1	79
	2500	5.4	84
	5000	3.1	97

4. Conclusions

A low-cost cellulose-based bioadsorbent (CRS) was obtained using the cellulosic material extracted from rose stems as the source of biomass. In the process, the corresponding precursor was treated with a mixture of acetic acid:nitric acid (v/v, 10:1) at 110 - 120 °C for 20 min. The final mixture was filtered and washed until a neutral pH was reached. The calculated crystallinity index from XRD measurements was 75 %, lower than the reported standard cellulose, this due to the contribution of the amorphous part characteristic of the cellulose structure and the other lignocellulosic structures. The TGA analysis showed a maximum decomposition peak corresponding to cellulose degradation at 321 °C. A slight shift, compared with the reported value for cellulose, was found probably related to the amorphous degree of the CRS sample. FTIR spectrum of CRS showed two signals, C=C at 1505 cm^{-1} and C-O at 1260 cm^{-1}, suggesting presence of traces of lignin and hemicellulose in the final product. Furthermore, SEM images showed undefined shapes, corresponding to lignocellulosic residues that remained in the sample, and the fiber surface was not regular, this was attributed to the acid treatment of fibers. FTIR, ^{13}C NMR, and XPS analyses showed signals of acetylation in the CRS sample. The treatment in an acid medium involved in the extraction of cellulose led to the cellulose sample generated being esterified. The adsorption process for the terbium removal from liquid effluents was investigated. An optimal pH of 5, with 80 % of terbium removal, was found. The increase of the adsorbent dosage improved the adsorption process, leading to a 92 % of adsorption when 1000 mg of the CRS sample was added. Increasing the temperature does not significantly improve the terbium adsorption process. Adsorption kinetic isotherms showed that the terbium adsorption was better described by the pseudo-second-order kinetic model at the different temperatures investigated. The experimental data were best fit to the Freundlich isotherm. Finally, the obtained activation energy value was 5.71 kJ/mol, which suggested that the terbium adsorption onto the CRS sample was a physical adsorption process. The obtained results in the present work revealed that the obtained low-cost adsorbent cellulose-based was useful for terbium adsorption from aqueous solutions. In addition, different desorption experiments showed that it was possible the effective recovery of terbium ions, from loaded adsorbent and using acid eluent solutions, with efficiencies of 80 - 97%.

Author Contributions: L.A., methodology, validation, formal analysis, investigation, writing-original draft preparation, writing review and editing; D.S., methodology, validation, formal analysis, investigation, writing-original draft preparation, writing review and editing; F.L., validation, formal analysis, investigation, writing-original draft preparation, writing review and editing; L.L., validation, formal analysis, investigation, writing-original draft preparation, writing review and editing; F.J.A., methodology, validation, formal analysis, investigation, writing-original draft preparation, writing review and editing; D.S., methodology, validation, formal analysis, investigation, writing-original draft preparation, writing review and editing; E.E., formal analysis; F.A.L., conceptualization; methodology investigation, writing-review and editing; funding adquisition; supervision; proyect administration.

Funding: This research has received funding from the European Union's Horizon 2020 research and innovation program under grant agreement Nº 776851 (Car-E Service).

Acknowledgments: Authors thank the agreement between Yachay Tech University (Ecuador) and the CSIC for doctoral students' stays at the CSIC. Authors from the National Center for Metallurgical Researches, Spanish National Research Council (CENIM-CSIC) would like to thank Dr. Irene Llorente for the XPS measurements carried out. Authors from Yachay Tech University thank support from project CHEM19-16.

Conflicts of Interest: The authors declare no conflict of interest.

References

1. M.I.A. Abdel Maksoud, A.M. Elgarahy, C. Farrell, A.H. Al-Muhtaseb, D.W. Rooney, A.I. Osman, Insight on water remediation application using magnetic nanomaterials and biosorbents, Coord. Chem. Rev. 403 (2020) 213096. doi:10.1016/j.ccr.2019.213096.
2. F.J. Alguacil, F.A. López, Adsorption Processing for the Removal of Toxic Hg(II) from Liquid Effluents: Advances in the 2019 Year, Metals (Basel). 10 (2020) 412. doi:10.3390/met10030412.

3. R. Ahmad, Z. Ali, A.A. Khan, N.U. Rehman, Terbium extraction by functionalized surface: experimental and DFT approach, Adsorption. 26 (2020) 117–125. doi:10.1007/s10450-019-00178-3.
4. H. Javadian, M. Ruiz, T.A. Saleh, A.M. Sastre, Ca-alginate/carboxymethyl chitosan/Ni0.2Zn0.2Fe2.6O4 magnetic bionanocomposite: Synthesis, characterization and application for single adsorption of Nd+3, Tb+3, and Dy+3 rare earth elements from aqueous media, J. Mol. Liq. 306 (2020) 112760. doi:10.1016/j.molliq.2020.112760.
5. H. Javadian, M. Ruiz, A.M. Sastre, Response surface methodology based on central composite design for simultaneous adsorption of rare earth elements using nanoporous calcium alginate/carboxymethyl chitosan microbiocomposite powder containing Ni0.2Zn0.2Fe2.6O4 magnetic nanoparticles: Batch, Int. J. Biol. Macromol. 154 (2020) 937–953. doi:10.1016/j.ijbiomac.2020.03.131.
6. H. Javadian, M. Ruiz, M. Taghavi, A.M. Sastre, Synthesis of magnetic CMC bionanocomposite containing a novel biodegradable nanoporous polyamide selectively synthesized in ionic liquid as green media: Investigation on Nd+3, Tb+3, and Dy+3 rare earth elements adsorption, J. Mol. Liq. 308 (2020) 113017. doi:10.1016/j.molliq.2020.113017.
7. B. Lapo, J.J. Bou, J. Hoyo, M. Carrillo, K. Peña, T. Tzanov, A.M. Sastre, A potential lignocellulosic biomass based on banana waste for critical rare earths recovery from aqueous solutions, Environ. Pollut. 264 (2020) 114409. doi:10.1016/j.envpol.2020.114409.
8. H. Javadian, M. Ruiz, M. Taghvai, A.M. Sastre, Novel magnetic nanocomposite of calcium alginate carrying poly(pyrimidine-thiophene-amide) as a novel green synthesized polyamide for adsorption study of neodymium, terbium, and dysprosium rare-earth ions, Colloids Surfaces A Physicochem. Eng. Asp. 603 (2020) 125252. doi:10.1016/j.colsurfa.2020.125252.
9. E.L. Afonso, L. Carvalho, S. Fateixa, C.O. Amorim, V.S. Amaral, C. Vale, E. Pereira, C.M. Silva, T. Trindade, C.B. Lopes, Can contaminated waters or wastewater be alternative sources for technology-critical elements? The case of removal and recovery of lanthanides, J. Hazard. Mater. 380 (2019) 120845. doi:10.1016/j.jhazmat.2019.120845.
10. M.A. Attia, S.I. Moussa, R.R. Sheha, H.H. Someda, E.A. Saad, Hydroxyapatite/NiFe2O4 superparamagnetic composite: Facile synthesis and adsorption of rare elements, Appl. Radiat. Isot. 145 (2019) 85–94. doi:10.1016/j.apradiso.2018.12.003.
11. H. Demey, T. Melkior, A. Chatroux, K. Attar, S. Thiery, H. Miller, M. Grateau, A.M. Sastre, M. Marchand, Evaluation of torrefied poplar-biomass as a low-cost sorbent for lead and terbium removal from aqueous solutions and energy co-generation, Chem. Eng. J. 361 (2019) 839–852. doi:10.1016/j.cej.2018.12.148.
12. J. Wang, Adsorption of aqueous neodymium, europium, gadolinium, terbium, and yttrium ions onto nZVI-montmorillonite: kinetics, thermodynamic mechanism, and the influence of coexisting ions, Environ. Sci. Pollut. Res. 25 (2018) 33521–33537. doi:10.1007/s11356-018-3296-0.
13. D. William, O. Connell, C. Birkinshaw, T. Francis, O. Dwyer, Heavy metal adsorbents prepared from the modification of cellulose : A review, 99 (2008) 6709–6724. doi:10.1016/j.biortech.2008.01.036.
14. A. Kosheleva, I. Atamaniuk, N. Politaeva, K. Kuchta, Adsorption of rare earth elements using bio-based sorbents, MATEC Web Conf. 245 (2018) 18001. doi:10.1051/matecconf/201824518001.
15. A. Negrea, A. Gabor, C.M. Davidescu, M. Ciopec, P. Negrea, N. Duteanu, A. Barbulescu, Rare Earth Elements Removal from Water Using Natural Polymers, Sci. Rep. 8 (2018) 316. doi:10.1038/s41598-017-18623-0.
16. L.S. Jeremy M. Berg, John L. Tymoczko, Gregory J. Gatto Jr., Biochemistry, 2015.
17. N. Kayra, A.Ö. Aytekin, Synthesis of Cellulose-Based Hydrogels: Preparation, Formation, Mixture, and Modification, in: 2018: pp. 1–28. doi:10.1007/978-3-319-76573-0_16-1.
18. A. Reghunadhan, N.G. Sivan, S. S. K., S.K. Mary, R.R. Koshy, J. Datta, S. Thomas, New-fangled sources of cellulose extraction: comparative study of the effectiveness of Cissus latifolia and Ficus benghalensis cellulose as a filler, Mater. Chem. Front. 3 (2019) 2025–2031. doi:10.1039/C9QM00431A.
19. S.M.F. Kabir, P.P. Sikdar, B. Haque, M.A.R. Bhuiyan, A. Ali, M.N. Islam, Cellulose-based hydrogel materials: chemistry, properties and their prospective applications, Prog. Biomater. 7 (2018) 153–174. doi:10.1007/s40204-018-0095-0.
20. L. Segal, J.J. Creely, A.E. Martin, C.M. Conrad, An Empirical Method for Estimating the Degree of Crystallinity of Native Cellulose Using the X-Ray Diffractometer, Text. Res. J. 29 (1959) 786–794. doi:10.1177/004051755902901003.

21. C.S.T. Araújo, I.L.S. Almeida, H.C. Rezende, S.M.L.O. Marcionilio, J.J.L. Léon, T.N. de Matos, Elucidation of mechanism involved in adsorption of Pb(II) onto lobeira fruit (Solanum lycocarpum) using Langmuir, Freundlich and Temkin isotherms, Microchem. J. 137 (2018) 348–354. doi:10.1016/j.microc.2017.11.009.
22. A.M. Aljeboree, A.N. Alshirifi, A.F. Alkaim, Kinetics and equilibrium study for the adsorption of textile dyes on coconut shell activated carbon, Arab. J. Chem. 10 (2017) S3381–S3393. doi:10.1016/j.arabjc.2014.01.020.
23. S. Lagergren, Zur Theorie der sogenannten Adsorption gelöster Stoffe, Zeitschrift Für Chemie Und Ind. Der Kolloide. 2 (1907) 15–15. doi:10.1007/BF01501332.
24. Y.. Ho, G. McKay, Pseudo-second order model for sorption processes, Process Biochem. 34 (1999) 451–465. doi:10.1016/S0032-9592(98)00112-5.
25. A.A. Inyinbor, F.A. Adekola, G.A. Olatunji, Kinetics, isotherms and thermodynamic modeling of liquid phase adsorption of Rhodamine B dye onto Raphia hookerie fruit epicarp, Water Resour. Ind. 15 (2016) 14–27. doi:10.1016/j.wri.2016.06.001.
26. F.J. Alguacil, F.A. Lopez, O. Rodriguez, S. Martinez-Ramirez, I. Garcia-Diaz, Sorption of indium (III) onto carbon nanotubes, Ecotoxicol. Environ. Saf. 130 (2016) 81–86. doi:10.1016/j.ecoenv.2016.04.008.
27. H.H. Mert, M.R. Moghbeli, S. Sajad, E.H. Mert, Functionalized cellulose nanocrytals (fCNCs) reinforced PolyHIPEs: Tailoring morphological, mechanical and thermal properties, React. Funct. Polym. 151 (2020) 104572. doi:10.1016/j.reactfunctpolym.2020.104572.
28. C. Jiao, Z. Zhang, J. Tao, D. Zhang, Y. Chen, H. Lin, Synthesis of a poly(amidoxime-hydroxamic acid) cellulose derivative and its application in heavy metal ion removal, RSC Adv. 7 (2017) 27787–27795. doi:10.1039/c7ra03365f.
29. S. Park, J.O. Baker, M.E. Himmel, P.A. Parilla, D.K. Johnson, Cellulose crystallinity index: measurement techniques and their impact on interpreting cellulase performance, Biotechnol. Biofuels. 3 (2010) 10. doi:10.1186/1754-6834-3-10.
30. J.X. Sun, X.F. Sun, H. Zhao, R.C. Sun, Isolation and characterization of cellulose from sugarcane bagasse, Polym. Degrad. Stab. 84 (2004) 331–339. doi:10.1016/j.polymdegradstab.2004.02.008.
31. J. Bian, F. Peng, X.-P. Peng, P. Peng, F. Xu, R.-C. Sun, Acetic acid enhanced purification of crude cellulose from sugarcane bagasse: Structural and morphological characterization, BioResources. 7 (2012). doi:10.15376/biores.7.4.4626-4639.
32. N. Johar, I. Ahmad, A. Dufresne, Extraction, preparation and characterization of cellulose fibres and nanocrystals from rice husk, Ind. Crops Prod. 37 (2012) 93–99. doi:10.1016/j.indcrop.2011.12.016.
33. D.L. Pavia, G.M. Lampman, G.S. Kriz, J.R. Vyvyan, Introduction to Spectroscopy, 4th ed., Washington, 2009.
34. M. Sasikala, M.J. Umapathy, Preparation and characterization of pineapple leaf cellulose nanocrystal reinforced gelatin bio-nanocomposite with antibacterial banana leaf extract for application in food packaging, New J. Chem. 42 (2018) 19979–19986. doi:10.1039/C8NJ02973C.
35. D. Watkins, M. Nuruddin, M. Hosur, A. Tcherbi-Narteh, S. Jeelani, Extraction and characterization of lignin from different biomass resources, J. Mater. Res. Technol. 4 (2015) 26–32. doi:10.1016/j.jmrt.2014.10.009.
36. K.A. Cychosz, M. Thommes, Progress in the Physisorption Characterization of Nanoporous Gas Storage Materials, Engineering. 4 (2018) 559–566. doi:10.1016/j.eng.2018.06.001.
37. G. Dorez, L. Ferry, R. Sonnier, A. Taguet, Journal of Analytical and Applied Pyrolysis Effect of cellulose , hemicellulose and lignin contents on pyrolysis and combustion of natural fibers, J. Anal. Appl. Pyrolysis. 107 (2014) 323–331. doi:10.1016/j.jaap.2014.03.017.
38. M.V. Kok, E. Ozgur, Environmental Effects Characterization of lignocellulose biomass and model compounds by thermogravimetry, Energy Sources, Part A Recover. Util. Environ. Eff. 39 (2017) 134–139. doi:10.1080/15567036.2016.1214643.
39. C. Liu, H. Wang, A.M. Karim, J. Sun, Y. Wang, Catalytic fast pyrolysis of lignocellulosic biomass, Chem. Soc. Rev. 43 (2014) 7594–7623. doi:10.1039/c3cs60414d.
40. H. Yang, R. Yan, H. Chen, D.H. Lee, C. Zheng, Characteristics of hemicellulose, cellulose and lignin pyrolysis, Fuel. 86 (2007) 1781–1788. doi:10.1016/j.fuel.2006.12.013.
41. C. Trilokesh, K. Babu Uppuluri, Isolation and characterization of cellulose nanocrystals from jackfruit peel, Mater. Lett. 129 (2014) 20–23. doi:10.1016/j.matlet.2014.05.019.
42. C.-F. Liu, R.-C. Sun, Cellulose, in: Cereal Straw as a Resour. Sustain. Biomater. Biofuels, 2010: pp. 131–167. doi:10.1016/B978-0-444-53234-3.00005-5.

43. S.S. Mohtar, T.N.Z. Tengku Malim Busu, A.M. Md Noor, N. Shaari, H. Mat, An ionic liquid treatment and fractionation of cellulose, hemicellulose and lignin from oil palm empty fruit bunch, Carbohydr. Polym. 166 (2017) 291–299. doi:10.1016/j.carbpol.2017.02.102.
44. S.S. Mohtar, T. Nur, Z. Tengku, M. Busu, A.M. Noor, N. Shaari, H. Mat, An ionic liquid treatment and fractionation of cellulose, hemicellulose and lignin from oil palm empty fruit bunch, Carbohydr. Polym. (2017). doi:10.1016/j.carbpol.2017.02.102.
45. S. Gan, S. Zakaria, C.H. Chia, R.S. Chen, A. V. Ellis, H. Kaco, Highly porous regenerated cellulose hydrogel and aerogel prepared from hydrothermal synthesized cellulose carbamate, PLoS One. 12 (2017) 1–13. doi:10.1371/journal.pone.0173743.
46. Y. Fu, G. Li, R. Wang, F. Zhang, M. Qin, Effect of the Molecular Structure of Acylating Agents on the Regioselectivity of Cellulosic Hydroxyl Groups in Ionic Liquid, BioResources. 12 (2016) 992–1006. doi:10.15376/biores.12.1.992-1006.
47. J.F. Moulder, W.F. Stickle, P.E. Sobol, K.D. Bomben, Handbook of X-ray Photoelectron Spectroscopy, Perkin-Elmer Corporation, United States of America, 1992.
48. T.N. Tran, U. Paul, J.A. Heredia-Guerrero, I. Liakos, S. Marras, A. Scarpellini, F. Ayadi, A. Athanassiou, I.S. Bayer, Transparent and flexible amorphous cellulose-acrylic hybrids, Chem. Eng. J. 287 (2016) 196–204. doi:10.1016/j.cej.2015.10.114.
49. A.J.S. Ahammad, N. Odhikari, S.S. Shah, M.M. Hasan, T. Islam, P.R. Pal, M.A. Ahmed Qasem, M.A. Aziz, Porous tal palm carbon nanosheets: Preparation, characterization and application for the simultaneous determination of dopamine and uric acid, Nanoscale Adv. 1 (2019) 613–626. doi:10.1039/c8na00090e.
50. F. Zhang, J. Dou, H. Zhang, Mixed membranes comprising carboxymethyl cellulose (as capping agent and gas barrier matrix) and nanoporous ZIF-L nanosheets for gas separation applications, Polymers (Basel). 10 (2018). doi:10.3390/polym10121340.
51. L.G. Wade, Wade Organic Chemistry 8e.pdf, 8th ed., United States of America, 2013.
52. J.R. Dorgan, B. Braun, J.R. Dorgan, Single-Step Method for the Isolation and Surface Functionalization of Cellulosic Nanowhiskers Article Single-Step Method for the Isolation and Surface Functionalization of Cellulosic Nanowhiskers, (2019). doi:10.1021/bm8011117.
53. Q. Xiang, Y. Lee, P. Pettersson, R. Torget, Heterogeneous Aspects of Acid Hydrolysis of a-Cellulose, in: Appl. Biochem. Biotechnol., Humana Press, Totowa, NJ, 2003: pp. 505–514. doi:https://doi.org/10.1007/978-1-4612-0057-4_42.
54. X. Yue, J. Huang, F. Jiang, H. Lin, Y. Chen, Synthesis and characterization of cellulose-based adsorbent for removal of anionic and cationic dyes, J. Eng. Fiber. Fabr. 14 (2019). doi:10.1177/1558925019828194.
55. I. Puigdomenech, Medusa program, (2020). www.kth.se/che/medusa.
56. P. Kampalanonwat, P. Supaphol, The Study of Competitive Adsorption of Heavy Metal Ions from Aqueous Solution by Aminated Polyacrylonitrile Nanofiber Mats, Energy Procedia. 56 (2014) 142–151. doi:10.1016/j.egypro.2014.07.142.
57. H. Javadian, S. Asadollahpour, M. Ruiz, A.M. Sastre, M. Ghasemi, S.M.H. Asl, M. Masomi, Using fuzzy inference system to predict Pb (II) removal from aqueous solutions by magnetic Fe3O4/H2SO4-activated Myrtus Communis leaves carbon nanocomposite, J. Taiwan Inst. Chem. Eng. 91 (2018) 186–199. doi:10.1016/j.jtice.2018.06.021.
58. M.Y. Abdelnaeim, I.Y. El Sherif, A.A. Attia, N.A. Fathy, M.F. El-Shahat, Impact of chemical activation on the adsorption performance of common reed towards Cu(II) and Cd(II), Int. J. Miner. Process. 157 (2016) 80–88. doi:10.1016/j.minpro.2016.09.013.
59. M.R. Malekbala, M.A. Khan, S. Hosseini, L.C. Abdullah, T.S.Y. Choong, Adsorption/desorption of cationic dye on surfactant modified mesoporous carbon coated monolith: Equilibrium, kinetic and thermodynamic studies, J. Ind. Eng. Chem. 21 (2015) 369–377. doi:10.1016/j.jiec.2014.02.047.
60. S. Rangabhashiyam, N. Anu, M.S. Giri Nandagopal, N. Selvaraju, Relevance of isotherm models in biosorption of pollutants by agricultural byproducts, J. Environ. Chem. Eng. 2 (2014) 398–414. doi:10.1016/j.jece.2014.01.014.
61. Y. Zhuang, J. Liu, J. Chen, P. Fei, Modified Pineapple Bran Cellulose by Potassium Permanganate as A Copper ion Adsorbent and Its Adsorption Kinetic and Adsorption Thermodynamic, Food Bioprod. Process. 122 (2020) 82–88. doi:10.1016/j.fbp.2020.04.008.

62. H.Y. Choi, J.H. Bae, Y. Hasegawa, S. An, I.S. Kim, H. Lee, M. Kim, Thiol-functionalized cellulose nanofiber membranes for the effective adsorption of heavy metal ions in water, Carbohydr. Polym. 234 (2020) 115881. doi:10.1016/j.carbpol.2020.115881.
63. E. Madivoli, P. Kareru, A. Gachanja, S. Mugo, M. Murigi, P. Kairigo, C. Kipyegon, J. Mutembei, F. Njonge, Adsorption of Selected Heavy Metals on Modified Nano Cellulose, Int. Res. J. Pure Appl. Chem. 12 (2016) 1–9. doi:10.9734/irjpac/2016/28548.
64. H.X. Zhu, X.J. Cao, Y.C. He, Q.P. Kong, H. He, J. Wang, Removal of Cu2+ from aqueous solutions by the novel modified bagasse pulp cellulose: Kinetics, isotherm and mechanism, Carbohydr. Polym. 129 (2015) 115–126. doi:10.1016/j.carbpol.2015.04.049.
65. A. Negrea, A. Gabor, C.M. Davidescu, M. Ciopec, P. Negrea, N. Duteanu, A. Barbulescu, Rare Earth Elements Removal from Water Using Natural Polymers, Sci. Rep. (2018) 1–11. doi:10.1038/s41598-017-18623-0.
66. M.A. Hubbe, S. Azizian, S. Douven, Implications of apparent pseudo-second-order adsorption kinetics onto cellulosic materials: A review, BioResources. 14 (2019) 7582–7626.
67. H.K. Boparai, M. Joseph, D.M. O'Carroll, Kinetics and thermodynamics of cadmium ion removal by adsorption onto nano zerovalent iron particles, J. Hazard. Mater. 186 (2011) 458–465. doi:10.1016/j.jhazmat.2010.11.029.